Journal of Materials Science & Technology 35 (2019) 1368–1377

Contents lists available at ScienceDirect

Journal of Materials Science & Technology

journal homepage: www.jmst.org

Research Article

Effects of samarium content on microstructure and mechanical properties of Mg–0.5Zn–0.5Zr alloy

Kai Guan[a,b,1], Fanzhi Meng[c,*,1], Pengfei Qin[a,d], Qiang Yang[a,*], Dongdong Zhang[a], Baishun Li[a], Wei Sun[a], Shuhui Lv[c], Yuanding Huang[e,*], Norbert Hort[e], Jian Meng[a,b]

[a] State Key Laboratory of Rare Earth Resource Utilization, Changchun Institute of Applied Chemistry, Chinese Academy of Sciences, Changchun 130022, China
[b] University of Science & Technology of China, Hefei 230026, China
[c] School of Materials Science and Engineering, Changchun University of Science and Technology, Changchun 130022, China
[d] Key Laboratory of Superlight Material and Surface Technology, Ministry of Education, College of Material Science and Chemical Engineering, Harbin Engineering University, Harbin 150001, China
[e] MagIC-Magnesium Innovation Centre, Helmholtz-Zentrum Geesthacht, Max-Planck Strasse 1, 21502, Geesthacht, Germany

ARTICLE INFO

Article history:
Received 26 December 2018
Received in revised form 18 January 2019
Accepted 19 January 2019
Available online 1 February 2019

Keywords:
Magnesium alloys
Samarium
Transmission electron microscopy (TEM)
Microstructure
Mechanical properties

ABSTRACT

Effects of samarium (Sm) content (0, 2.0, 3.5, 5.0, 6.5 wt%) on microstructure and mechanical properties of Mg–0.5Zn–0.5 Zr alloy under as-cast and as-extruded states were thoroughly investigated. Results indicate that grains of the as-cast alloys are gradually refined as Sm content increases. The dominant intermetallic phase changes from Mg_3Sm to $Mg_{41}Sm_5$ till Sm content exceeds 5.0 wt%. The dynamically precipitated intermetallic phase during hot-extrusion in all Sm-containing alloys is Mg_3Sm. The intermetallic particles induced by Sm addition could act as heterogeneous nucleation sites for dynamic recrystallization during hot extrusion. They promoted dynamic recrystallization via the particle stimulated nucleation mechanism, and resulted in weakening the basal texture in the as-extruded alloys. Sm addition can significantly enhance the strength of the as-extruded Mg–0.5Zn–0.5 Zr alloy at room temperature, with the optimal dosage of 3.5 wt%. The optimal yield strength (YS) and ultimate tensile strength (UTS) are 368 MPa and 383 MPa, which were enhanced by approximately 23.1% and 20.8% compared with the Sm-free alloy, respectively. Based on microstructural analysis, the dominant strengthening mechanisms are revealed to be grain boundary strengthening and dispersion strengthening.

1. Introduction

With the ever-increasing emphases on environmental protection and energy conservation, magnesium (Mg) alloys as light structural metallic materials exhibit significant advantages in automotive and aerospace industries owing to their low density, good damping property and high specific strength [1–3]. Unfortunately, their insufficient strength, poor formability and corrosion resistance restrict their extensive applications. It is well known that alloying is one of the most effective approaches to improve the strength of Mg alloys. In recent years, Mg–RE (rare earth) alloys have attracted a great deal of attention, because the addition of RE elements can remarkably refine microstructure, effectively promote the formation of thermostable particles, and consequently improve the alloy's mechanical properties [4–18]. Among various Mg–RE systems, Mg–RE–Zn–Zr is one of the most representative high-strength systems, where Zn can significantly increase the aging strengthening, and Zr can obviously refine grains [15–17].

It is reported that the maximum solid solubility of Sm is 5.8 wt% at eutectic temperature 530 °C in Mg. It could decrease sharply with a drop of temperature. This means that Sm addition provides favorable solid-solution strengthening and precipitation strengthening [7,19–22]. Additionally, Sm is cheaper than other RE elements frequently used in high-strength Mg–RE-based alloys, such as Gd, Y and Nd. Yang et al. [20,23] reported that Sm addition can remarkably enhance precipitation strengthening in a die-cast Mg–Al-based alloy. Sun et al. [24] reported that Sm can obviously refine the microstructure of an as-cast Mg–3Al–1Zn–0.3 Mn alloy and remarkably improve the alloy's tensile properties. Li et al. [21]

* Corresponding authors.
E-mail addresses: fzmeng@ciac.ac.cn (F. Meng), qiangyang@ciac.ac.cn (Q. Yang), yuanding.huang@hzg.de (Y. Huang).
[1] These authors contributed equally to this work.

https://doi.org/10.1016/j.jmst.2019.01.019
1005-0302/

Table 1
Chemical composition of the presented alloys (wt%).

Alloy	Sm	Zn	Zr	Mg	Fe	Si
A	–	0.57	0.45	Bal.	0.0014	0.0211
B	2.04	0.65	0.53	Bal.	0.0023	0.0173
C	3.33	0.55	0.46	Bal.	0.0015	0.0186
D	4.87	0.56	0.56	Bal.	0.0018	0.0053
E	6.31	0.54	0.51	Bal.	0.0019	0.0059

demonstrated that extruded Mg–4Sm alloy exhibits remarkable age hardening responses. Afterwards, Xia et al. investigated the precipitation evolution and its hardening effect in a newly-developed Mg–Sm–Zn–Zr alloy [7].

As is well known, the intermetallic phases formed during solidification have a significant influence on microstructure and mechanical properties of as-extruded products. However, some inconsistencies exist on the crystal structures of the dominant intermetallic phase in Mg–Sm–Zn–Zr alloys. Su et al. [25] and Zheng et al. [26] reported that the dominant intermetallic phase in as-cast Mg–Sm–Zn–Zr alloys is $Mg_{41}Sm_5$. Yuan and Zheng [27] reported that the dominant intermetallic phase in as-cast Mg–2.6Sm–1.3Gd–0.6Zn–0.5 Zr alloy is Mg_3RE other than $Mg_{41}RE_5$ (RE = Sm, Gd). Lyu et al. [28] indicated that the dominant intermetallic phase in high-hardness casting Mg–7Y–5Sm–0.5Zn–0.3 Zr alloy is $(Mg,Zn)_3(Y,Sm)$. Recently, our work shows that the dominant intermetallic phase in as-cast Mg–3.5Sm–0.6Zn–0.5 Zr alloy is Mg_3Sm [18]. Therefore, the relationships between the crystal structure of the dominant intermetallic phase and the Sm content still remain blank. Furthermore, microstructure and the corresponding mechanical properties of the as-extruded Mg–Sm–Zn–Zr alloys with various Sm contents have been scarcely investigated to date. According to our previous work, hot-extruded Mg–3.5Sm–0.6Zn–0.5 Zr alloy exhibits high strength [18]. Therefore, investigating the influences of Sm content on microstructure and mechanical properties of Mg–Sm–Zn–Zr alloys is very important to develop high-strength Mg alloys.

In the present work, the crystal structure of the dominant intermetallic phases in as-cast Mg–*x*Sm–0.5Zn–0.5 Zr (*x* = 0, 2.0, 3.5, 5.0, and 6.5) alloys was investigated systematically. The influences of various Sm additions on the microstructures and mechanical properties were studied for the as-extruded alloys. The strengthening mechanisms were explored and discussed.

2. Experimental

The experimental alloys with nominal compositions of Mg–*x*Sm–0.5Zn–0.5 Zr (*x* = 0, 2.0, 3.5, 5.0, and 6.5) were fabricated using commercial pure Mg, Mg–20Sm (wt%) master alloy, Mg–30Zr (wt%) master alloy and commercial pure Zn in a mild steel crucible installed in an electrical resistance furnace under mixed protective atmosphere of 1 vol.% SF_6 and 99 vol.% CO_2. Until heated to 750–760 °C, the molten alloys were mechanically stirred for 8–10 min and subsequently held for 25–35 min. Afterward, the molten alloys were cooled down to 710–720 °C, before pouring into a preheated mild steel mold with 90 mm diameter. Cylindrical billets with approximately 82 mm in diameter were machined from the as-cast ingots for subsequent extrusion. Prior to extrusion, the cylindrical billets were preheated at 320 °C for about 2 h. Finally, the extrusion experiments were conducted at the same temperature.

The actual chemical compositions of the fabricated alloys were measured using inductively coupled plasma atomic emission spectroscopy (ICP-AES) (Table 1). The microstructures were investigated using optical microscopy (OM, Olympus-GX71) and backscatter scanning electron microscopy (SEM, Hitachi S-4800) with an accelerating voltage of 10 kV. The intermetallic phases were identified by X-ray diffractometer (XRD, Bruker D8 FOCUS) using Cu*Kα* radiation (wavelength = 0.15406 nm) at 40 kV and 40 mA with scanning speed of 2°/min, and transmission electron microscopy (TEM, FEI Tecnai G^2 F20) equipped with an EDAX energy dispersive spectroscopy (EDS) operating at 200 kV. For OM and SEM characterizations, the polished samples were etched using a mixed solution of 1 g picric acid, 1 ml acetic acid, 20 ml ethanol and 2 ml H_2O. Thin TEM foils with 3 mm in diameter were mechanically grounded to about 50 μm and then ion-beam milled by a Gatan 691 precision ion polishing system. The grain sizes of the specimens were measured using Nano Measurer software.

Cylindrical tensile samples were machined from the extruded rods paralleling to the extrusion direction, with the gauge radius and the gauge length of 3 mm and 36 mm (close to the samples for sub-size ASTM B557 standard), respectively. Tensile tests were carried out with an initial strain rate of 1.0×10^{-3} s^{-1} at ambient temperature, which was in compliance with ISO 9513 standards. To ensure the reproducibility, the measurements were repeated at least three times for each testing condition and the results presented in this work are the average.

3. Results and discussion

3.1. Microstructures of the as-cast alloys

Fig. 1(a)–(e) shows OM micrographs of as-cast Mg–0.5Zn–0.5 Zr alloys with different Sm contents. Their corresponding average grain sizes were presented in Fig. 1(f). As Sm content increases, the grain size monotonously decreases. This indicates that Sm addition has a satisfactory grain refinement effect. After Sm addition, the accumulation of Sm atoms near the solid–liquid interface would lead to constitutional super-cooling, finally accelerated the nucleation of *α*-Mg during solidification [29,30]. Furthermore, more Sm addition results in much greater constitutional super-cooling. Thus, the alloys with more Sm addition have obviously finer grains. In addition, Fig. 1(a)–(e) demonstrates that more and more intermetallic particles are formed at grain boundaries as Sm addition increases, which can further be seen more clearly from the corresponding SEM micrographs (Fig. 2(a)–(e)). In the alloy without Sm addition, almost no intermetallic phases were observed at grain boundaries except for a few granular particles dispersed inside *α*-Mg grains. After 2 wt% Sm addition, the lamellae intermetallic particles can be clearly observed at the triangle grain boundaries. As Sm addition increases to 3.5 wt%, much more intermetallic particles are found at grain boundaries and their size becomes greater. Among them, the relatively coarser intermetallic particles present reticular while the relatively finer ones are still lamellae. As the addition increases to 5.0 wt% and 6.5 wt%, both reticular and lamellae intermetallic phases can be observed and they become more and more. Fig. 2(f) gives the statistic volume fraction of intermetallic compounds versus Sm content. It is obvious that volume fraction of the intermetallic compounds increases monotonously with Sm content increases. Generally, in-situ formed intermetallic particles preferentially nucleate at grain boundaries during solidification, subsequently act as effective obstacles to restrict grain boundary migration during grain growth [15]. Therefore, more Sm additions result in finer grains. It should be noted that the increasing rate in volume fraction of intermetallics suddenly becomes much greater when the Sm addition is over 5.0 wt%. For example, the volume fraction increment is only 2.56% when Sm addition increases from 3.5 wt% to 5.0 wt%. However, when Sm addition increases from 5.0 wt% to 6.5 wt%, volume fraction increment of the intermetallic compounds is 9.1%. This will be discussed in detail in the following paragraphs.

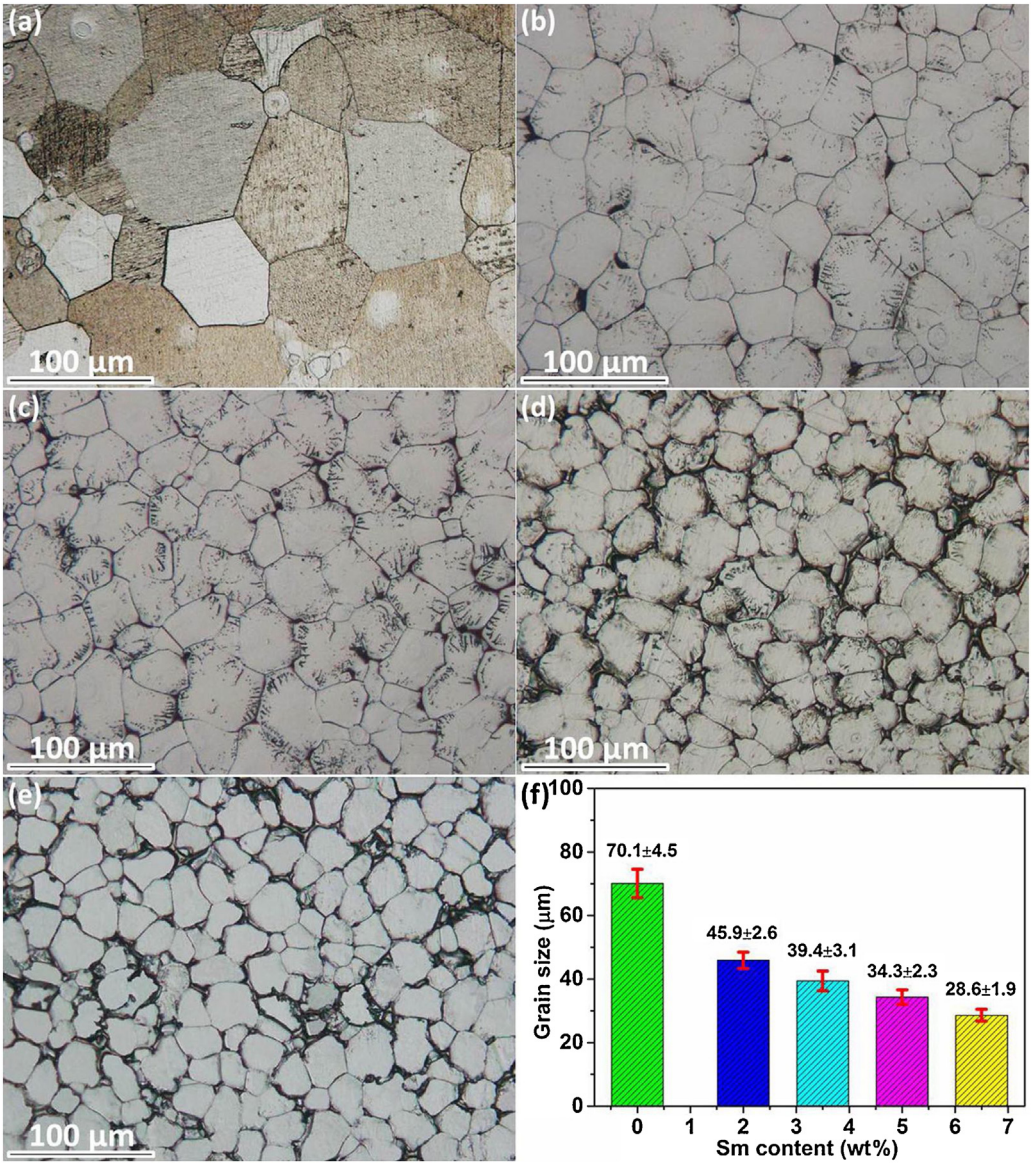

Fig. 1. OM micrographs of as-cast alloys of (a) alloy A, (b) alloy B, (c) alloy C, (d) alloy D, (e) alloy E and (f) average grain size.

Fig. 3 shows XRD patterns obtained from these five alloys. In the alloy with free Sm addition, no obvious additional diffraction peaks except for those from α-Mg are identified. This confirms that the amount of intermetallic phase in A alloy is very low, which is consistent with OM and SEM observations. After Sm addition, the alloys mainly contain strong diffraction peaks consistent with α-Mg matrix and some additional diffraction peaks from the intermetallic phases. When the Sm addition is below 5.0 wt%, the additional diffraction peaks can basically be indexed as Mg_3Sm (face-centered cubic crystal structure, lattice parameter $a = 0.7371$ nm). The intensity of the diffraction peaks increases with increasing Sm content, indicating that volume fraction of the intermetallic compound Mg_3Sm increases as Sm content increases. This is in line with the microstructural observations (Fig. 2). Interestingly, after 6.5 wt% Sm addition, the diffraction peaks from intermetallic phase cannot be reasonably indexed as Mg_3Sm. Their identification is replaced with $Mg_{41}Sm_5$ (primitive tetragonal crystal structure, $a = 1.476$ nm and $c = 1.039$ nm). In summary, the dominant intermetallic phase in Mg–Sm–Zn–Zr system is closely related to Sm content, which was not reported in the previous open literature. As shown in Fig. 3, intensity of $Mg_{41}Sm_5$ diffraction peaks is obviously stronger than that of Mg_3Sm phase, demonstrating its higher volume fraction. This is in line with the SEM analysis result. According to the chemical formulas, the formation of $Mg_{41}Sm_5$ consumes much more Mg atoms than that of Mg_3Sm. With respect to the same Sm atoms, $Mg_{41}Sm_5$ phase has a much greater volume than Mg_3Sm phase. When Sm content is below 5.0 wt%, Sm addition is consumed to form Mg_3Sm. While in the alloy with 6.5 wt% Sm addition, all Sm atoms except for those dissolved in α-Mg matrix were consumed to form $Mg_{41}Sm_5$. This leads to a sudden increase in the volume fraction of intermetallic compounds when Sm addition increases from 5.0 wt% to 6.5 wt%.

To identify crystallographic structures of the dominant intermetallic particles in detail, TEM characterizations were used. According to TEM observations, both reticular and lamellae intermetallic phases in the same alloy have the same crystal structures. Fig. 4 shows the representative bright-field TEM (BF-TEM) images along with the selected area electronic diffraction (SAED) patterns and the corresponding EDS spectra. The results (Fig. 4(a)–(l)) manifest that the dominant intermetallic phase in the alloy with Sm addition below 5.0 wt% is Mg_3Sm, and their experimental lattice parameters are approximately same. Fig. 4(m) presents the repre-

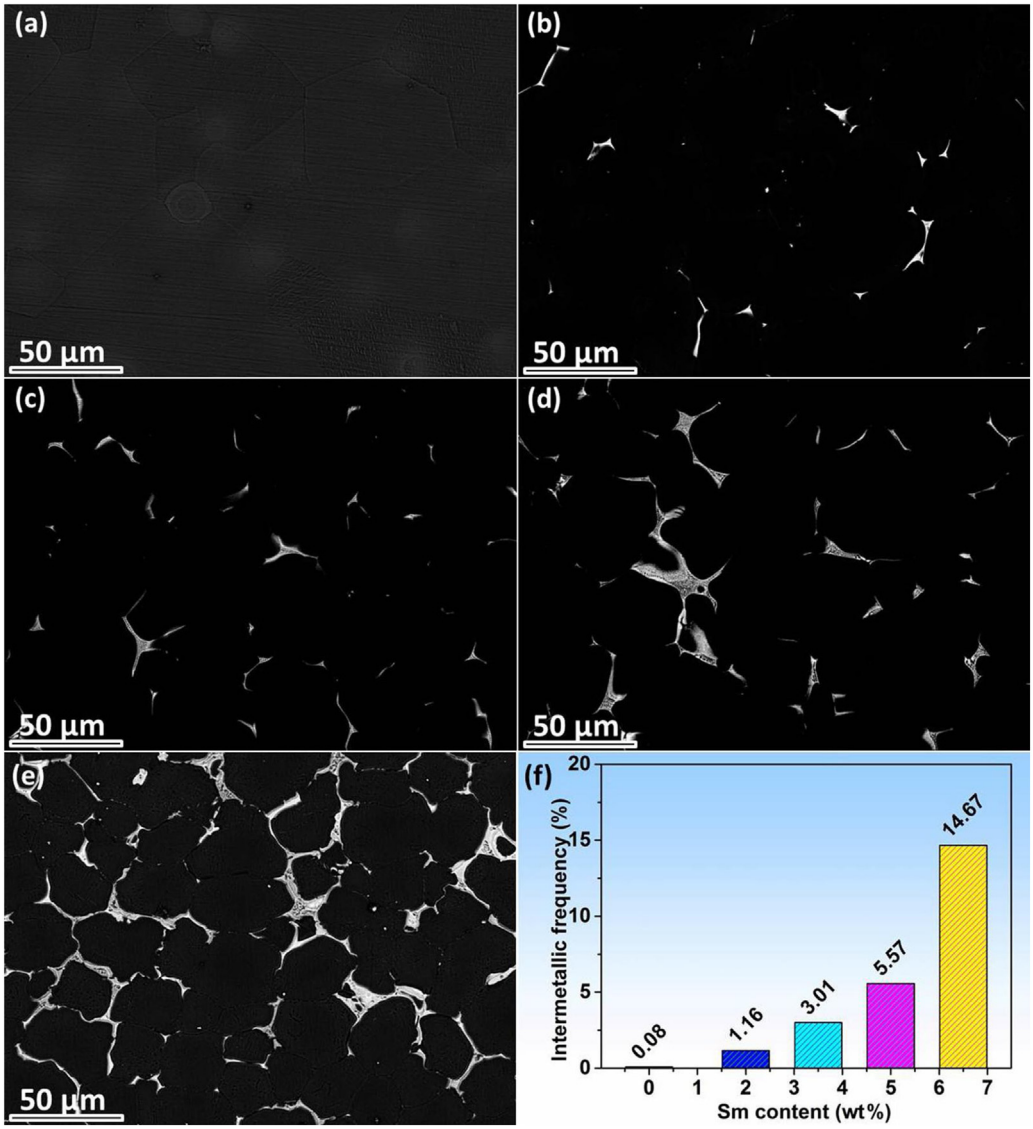

Fig. 2. SEM micrographs of as-cast alloys of (a) alloy A, (b) alloy B, (c) alloy C, (d) alloy D, (e) alloy E and (f) volume frequency of intermetallic compounds.

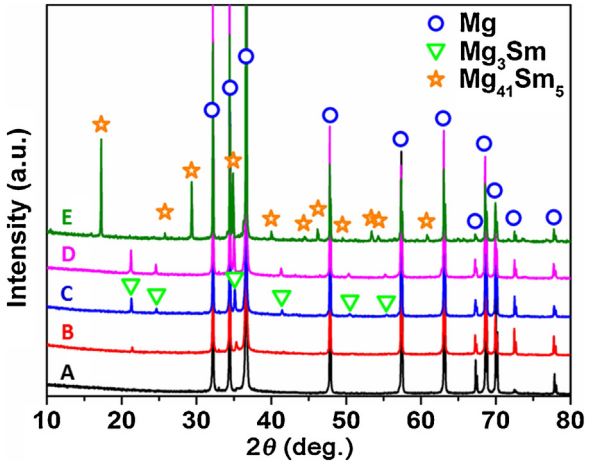

Fig. 3. XRD patterns of as-cast samples.

sentative BF-TEM micrograph of the network-shaped intermetallic phase in as-cast E alloy. There are no obvious differences on morphologies between the two reticular phases in alloys D (Fig. 4(i)) and E. However, the corresponding SAED patterns (Fig. 4(n) and (o)) indicate that the reticular intermetallic phase in E alloy is $Mg_{41}Sm_5$ other than Mg_3Sm, It is of interest to note, the point EDS analysis results (Fig. 4(d), (h), (l), (p)) illustrate that Mg_3Sm phase is with a relatively high Zn concentration while only a few of Zn in $Mg_{41}Sm_5$ phase. The similar phenomenon has been reported by Xia et al. in Mg–Sm–Zn system [8], where Mg_3Sm phase with a relatively large solubility of Zn was observed in Mg–12.14Sm–9.45Zn alloy although $Mg_{41}Sm_5$ phase was confirmed in Mg–13.01Sm–1.17Zn alloy. Therefore, it can be deduced that the ratio of Zn:Sm might have a decisive influence on the formation of Mg_3Sm and $Mg_{41}Sm_5$ during solidification.

3.2. Microstructures of the as-extruded alloys

The representative SEM micrographs in longitudinal section of the as-extruded A-E alloys are presented in Fig. 5(a)–(e), respectively. All alloys are composed of fine equiaxed dynamic recrystallization (DRX) grains and relatively coarse unrecrystallized grains distorted along the extrusion direction (ED). With respect to the alloy with free Sm addition, the average DRX grain size is approximately 3 μm. After Sm addition, the fraction of

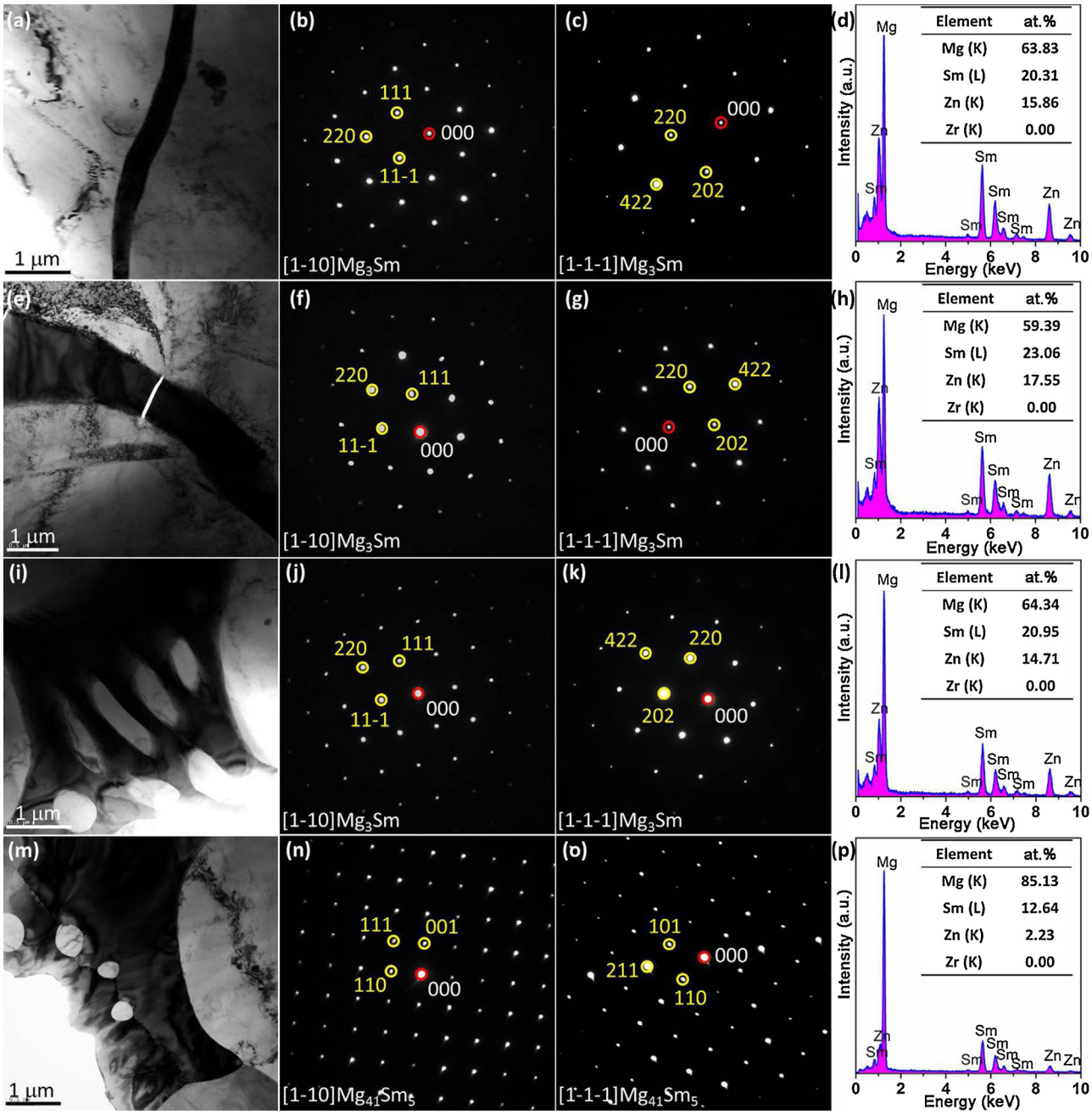

Fig. 4. BF-TEM images (a, e, i, m), corresponding SAED patterns (b, c, f, g, j, k, n, o) and EDS spectra (d, h, l, p) of as-cast alloys of (a-d) alloy B, (e-h) alloy C, (i-l) alloy D and (m-p) alloy E.

DRX area increases and the DRX grains become too much finer to identify their sizes according to SEM observations. Additionally, well defined extrusion stringers along ED with numerous disintegrated intermetallic phase fragments can be clearly observed after Sm addition. Fig. 5(f) gives the statistic results of the average width of extrusion stringers and the average size of disintegrated intermetallic particles distributed at stringers. As the Sm content increases, the width of extrusion stringers becomes greater and the disintegrated intermetallic particles at extrusion stringers are much coarser, particularly for the alloy with 6.5 wt% Sm addition. The evolution characteristics of extrusion stringers might be attributed to the increase in intermetallic compounds in the as-cast samples.

It is noted that there are a great number of finer intermetallic particles distributed in the DRX regions of as-extruded alloys B-E while almost no ones in as-extruded alloy A, which can be seen more clearly in high angle annular dark field scanning TEM (HAADF-STEM) images (Fig. 6(a)–(e)). In the as-extruded alloy A (Fig. 6(a)), DRX grains were clearly observed and no intermetallic particles were found. After Sm addition (Fig. 6(b)), the dynamically precipitated intermetallic particles were observed and mainly distributed at/near DRX grain boundaries. Their average size is approximately 100 nm. As Sm content increases to 3.5 wt% (Fig. 6(c)), there are much more dynamically precipitated intermetallic particles in the DRX regions although their size slightly increases, with an average size of approximately 130 nm. As Sm content reaches to 5.0 wt% (Fig. 6(d)), there are a comparative number density of the dynamically precipitated intermetallic particles with that in the as-extruded alloy containing 3.5 wt% Sm addition. However, the dynamically precipitated particles have clearly a greater aver-

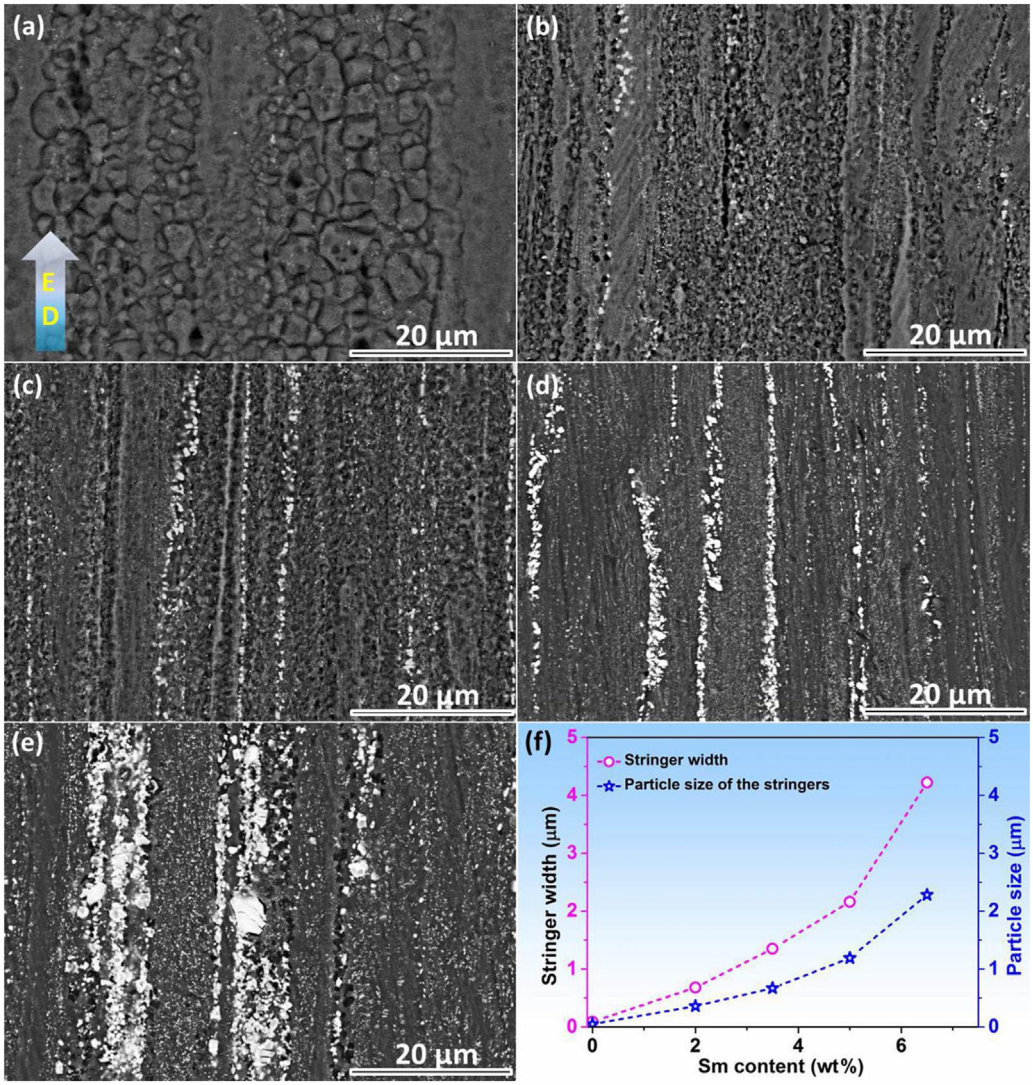

Fig. 5. SEM micrographs of as-extruded alloys of (a) alloy A, (b) alloy B, (c) alloy C, (d) alloy D, (e) alloy E and (f) stringer width and particle size of stringers as a function of Sm content.

age size of approximately 240 nm. When Sm content is 6.5 wt% (Fig. 6(e)), many relatively coarse blocky intermetallic compounds distributed in the DRX regions although a number of fine precipitates can also be observed.

The DRX grains can be well distinguished from TEM observations. Fig. 6(f) shows the statistic histogram of the average DRX grain size in as-extruded alloys A-E. Different from that more Sm addition results in finer grains in the as-cast samples, the DRX grain size firstly decreases as Sm addition increases but then starts to increase when Sm content is over 3.5 wt%. It is widely reported that RE additions in Mg alloys promote DRX during hot extrusion based on the particle stimulated nucleation (PSN) mechanism [19,31–33]. That means that the dispersed intermetallic particles induced by Sm addition can act as heterogeneous nucleation sites for recrystallization through generating local inhomogeneity of strain energy and enhancing driving force of recrystallization. Simultaneously, these dispersed particles can also effectively refine the DRX grains via pinning up grain boundary. Amounts of intermetallic particles finely distributed in grain boundaries play a significant role in suppressing the growth of DRX grains. In this work, as Sm content increases, there are more and more intermetallic particles. These particles can promote DRX via the classical PSN mechanism. As a result, more Sm addition leads to finer DRX grains when Sm addition is below 3.5 wt%. However, it should also be noted that the large intermetallic particles would shelter α-Mg when deformation occurs [34]. This results in smaller strain accumulation of α-Mg matrix, thus lowers strain energy, i.e. smaller driving force for recrystallization. Thus, too many intermetallic particles in the as-cast sample are possibly not in favor of promoting DRX. Consequently, the alloy with 6.5 wt% Sm addition has larger DRX grains than that with few Sm additions.

3.3. *Intermetallic phases in the as-extruded alloys*

Fig. 7 shows XRD patterns of the as-extruded alloys. There are no obvious diffraction peaks from intermetallic phases for the as-extruded A alloy. This indicates that no intermetallic phases were dynamically precipitated in A alloy during hot-extrusion. The dominant intermetallic phase in the as-extruded B-D alloys remains. As indicated by the SEM images (Fig. 5(b)–(d)) and HAADF-STEM images (Fig. 6(b)–(d)), amounts of precipitates were dynamically formed in the DRX regions. XRD results suggest that the fine dynamically precipitates in the as-extruded B-D alloys are still Mg_3Sm. With respect to as-extruded E alloy, some diffraction peaks corresponding to Mg_3Sm appear after hot-extrusion. This demonstrates that the fine dynamically precipitates in the as-extruded E alloy

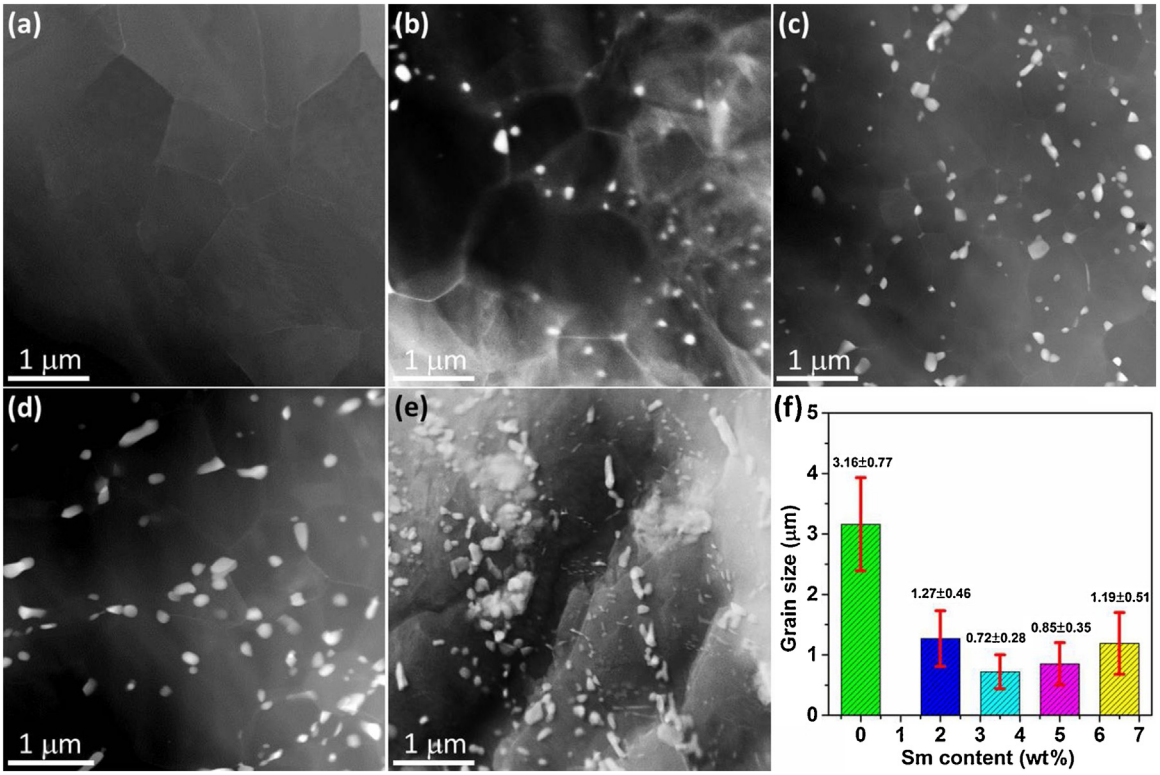

Fig. 6. HAADF-STEM images of as-extruded samples of (a) alloy A, (b) alloy B, (c) alloy C, (d) alloy D, (e) alloy E and (f) statistic grain diameter distributions in form of histogram for DRX grains.

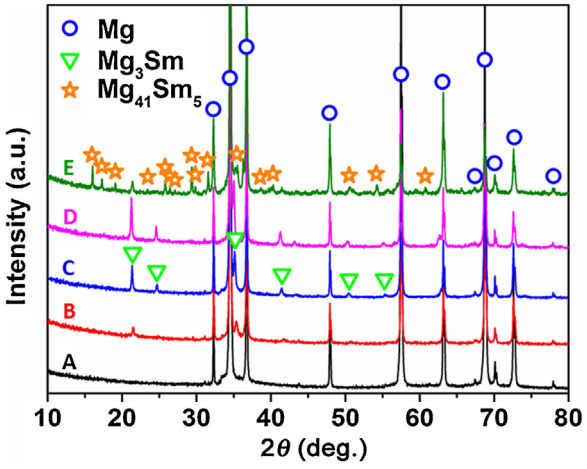

Fig. 7. XRD patterns of as-extruded alloys.

may also be Mg_3Sm, but it cannot be excluded that a part of $Mg_{41}Sm_5$ phase transformed to Mg_3Sm during extrusion. In order to well identify the crystal structures of the intermetallic phases, TEM observations were performed on the as-extruded samples. Fig. 8 shows the typical BF-TEM images (Fig. 8(a)–(c)) along with the corresponding SAED patterns (Fig. 8(d)–(f)) of fine precipitates in the DRX region, the discrete coarse intermetallic phase and the disintegrated intermetallic phase at extrusion stringers, respectively. The results illustrate that all above three typed intermetallic phases are Mg_3Sm. Fig. 9 presents the representative HAADF-STEM image of disintegrated intermetallic phases along with the dynamically precipitated intermetallic phase near the extrusion stringer in the as-extruded E alloy. According to the corresponding SAED patterns (Fig. 9(b) and (c)), the dynamically precipitated intermetallic phase is not $Mg_{41}Sm_5$ but Mg_3Sm while the coarse disintegrated intermetallic phase at the extrusion stringers is still $Mg_{41}Sm_5$. In this work, the coexistence of $Mg_{41}Sm_5$ and Mg_3Sm was not found during amounts of TEM observations. Thus, $Mg_{41}Sm_5$ phase is thermodynamically stable and would not transform to Mg_3Sm during bot-extrusion at 320 °C. Fig. 9(d) illustrates the EDS mapping images corresponding to the region marked by a yellow dotted box. It is obvious that Zn is mainly enriched in the dynamically precipitated Mg_3Sm phase while only a few of Zn in the $Mg_{41}Sm_5$ phase. Fig. 9(e) and (f) gives EDS spectra along with the analysis results for $Mg_{41}Sm_5$ and Mg_3Sm phases, respectively. The results demonstrate that the atomic ratio of Mg:(Sm, Zn) is approximately 2.61 and 8.87, respectively. This further confirms that the dynamically precipitated intermetallic phase in the as-extruded E alloy is Mg_3Sm while the disintegrated intermetallic phase is $Mg_{41}Sm_5$.

3.4. Texture evolution in the as-extruded alloys

It is well known that basal texture is always formed during hot extrusion in Mg alloys [9,10,35–39]. XRD was performed to explore the texture evolution of as-extruded A-E alloys, and results are shown in Fig. 10. It is evident that intensity of the diffraction peaks corresponding to the (0002) basal plane is much higher than that of $(10\bar{1}0)$ prismatic plane and $(10\bar{1}1)$ pyramidal plane. The relative intensity (I%) of diffraction peaks can be calculated by the following equations [36]:

$$I = \frac{I_{\{hkil\}}}{\sum I_{\{hkil\}}} \quad (1)$$

$$\sum I_{\{hkil\}} = I_{\{10\bar{1}0\}} + I_{\{0002\}} + I_{\{10\bar{1}1\}} \quad (2)$$

The relative intensity of (0002) diffraction peak ($I_{(0002)}$) corresponding to the as-extruded A-E alloys are 88.74%, 77.89%, 75.49%, 72.16% and 65.65%, respectively. The results reveal that the rela-

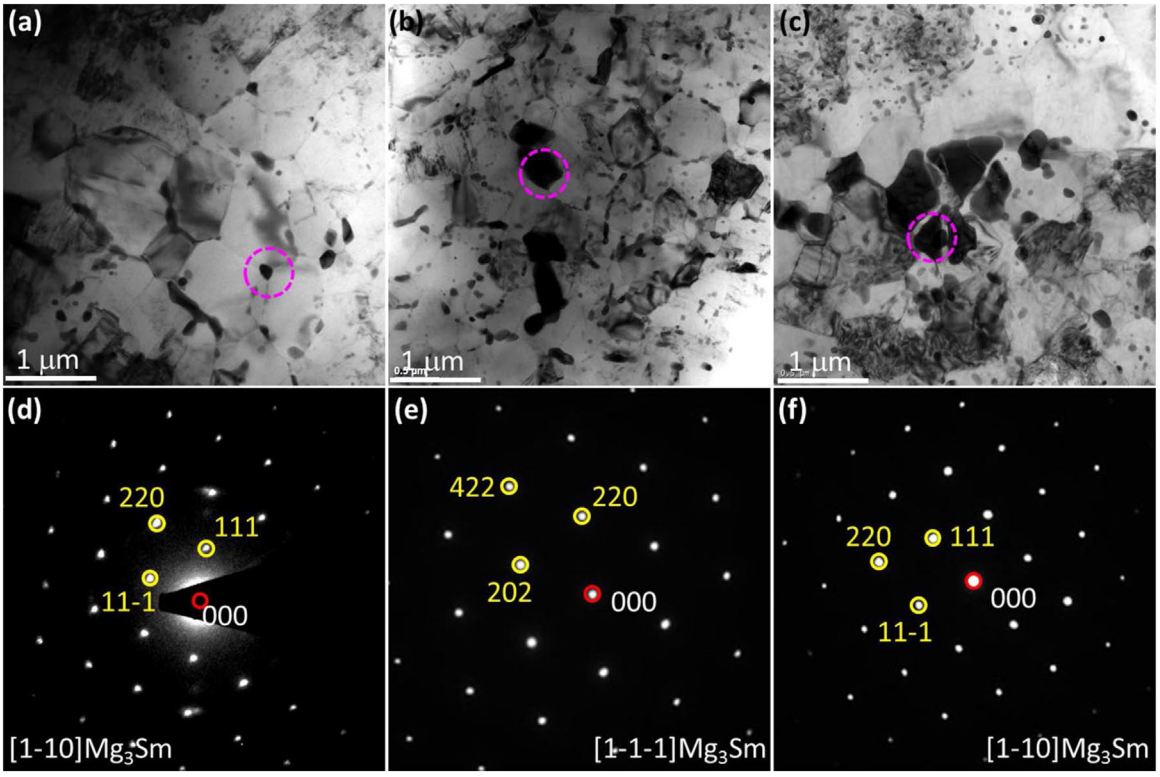

Fig. 8. (a-c) BF-TEM images and (d-f) corresponding SAED patterns of as-extruded alloys of (a, d) alloy B, (b, e) alloy C, and (c, f) alloy D.

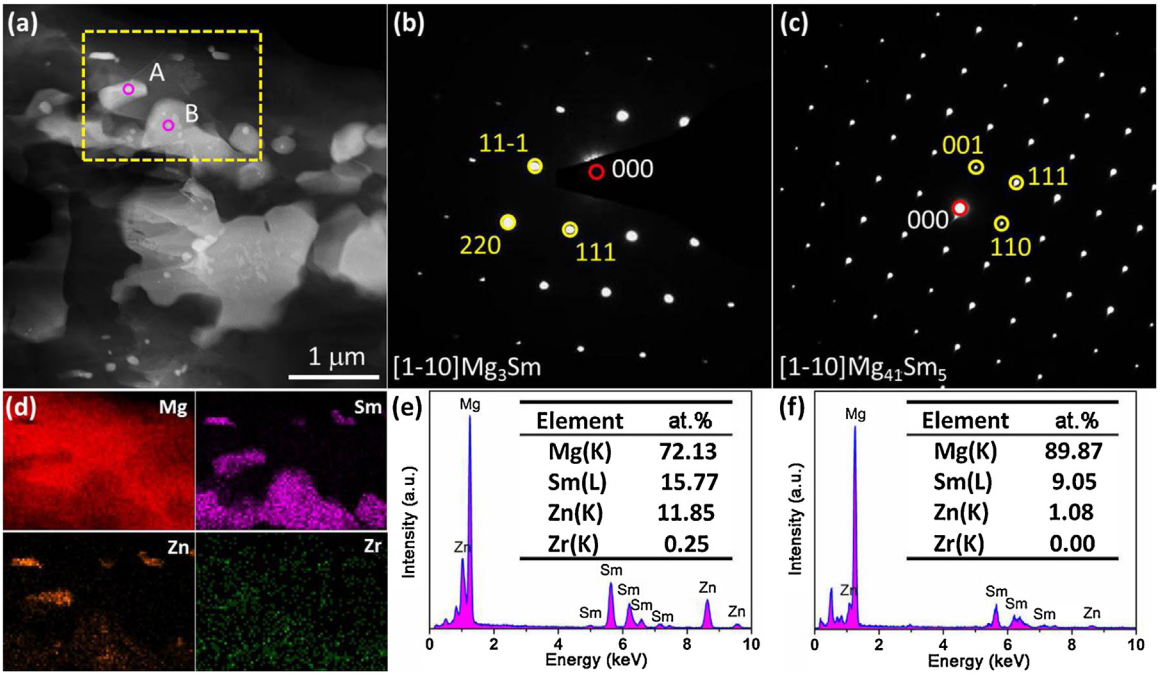

Fig. 9. (a) HAADF-STEM image of as-extruded alloy E, (b, c) corresponding SAED patterns and (d) EDS mappings along with (e, f) corresponding point EDS spectra.

tively strong basal texture was produced in the studied alloys, and the intensity decreases monotonously as the Sm content increases. It was reported that DRX grains exhibit a weak basal texture in Mg-RE based alloys after hot extrusion, while the unrecrystallized grains exhibit a strong basal texture [35,37–39]. Therefore, the volume fraction of unrecrystallized regions plays an important role in affecting texture performance. According to Fig. 5, the volume fraction of unrecrystallized regions decreases as Sm content increases. Therefore, the weakness of basal texture in the studied alloys is mainly attributed to the greater DRX degree.

3.5. Mechanical properties of the as-extruded alloys

Fig. 11 presents the ambient temperature tensile properties, including tensile yield strength (YS), ultimate tensile strength (UTS), and elongation (EL), of the as-extruded alloys. The results

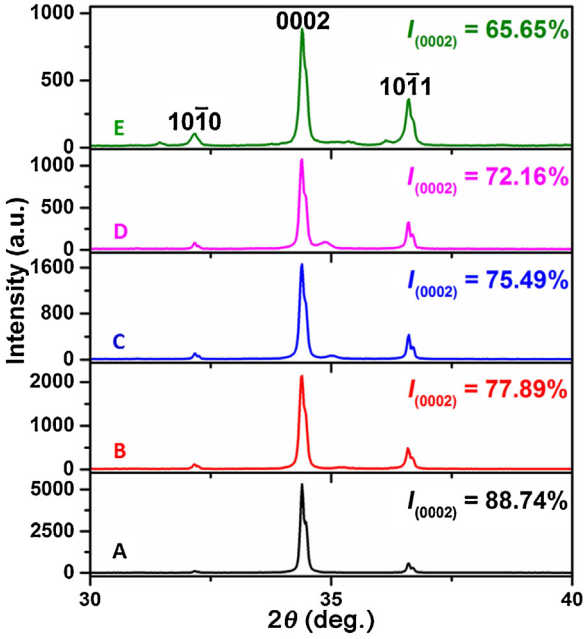

Fig. 10. Relative intensities of peaks corresponding to basal (0002) plane of as-extruded samples.

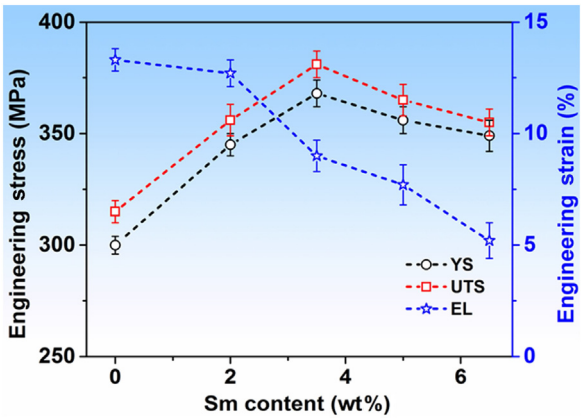

Fig. 11. Tensile properties of as-extruded alloys.

indicate that Sm addition can significantly enhance YS and UTS of the as-extruded alloys, whereas ε gradually decreases. The reduction in ε with increase in Sm content is mainly attributed to the increasing size of particles distributed at extrusion stringers as presented in Fig. 5(f). The relative coarse intermetallic particles may weaken the interface between α-Mg matrix and particles, resulting in micro-crack during the deformation. Similar explanations were also reported by Yu et al. [31] in Mg–6Zn–0.5 Zr–*x*Ce (*x* = 0, 0.5, 1.0, and 1.5 wt%) alloys. Moreover, it is interesting to note that with increase in Sm content, both YS and UTS increase first and then decrease, although all of them are much higher than those of Sm-free alloy A. The as-extruded alloy C containing 3.5 wt% Sm displays optimal YS (368 MPa) and UTS (383 MPa), which are enhanced by approximately 23.1% and 20.8% compared with alloy A with free Sm addition, respectively. As shown in Fig. 6f, the grain size of the DRX regions in these as-extruded alloys is remarkably refined due to Sm addition. It is well known that the grain size refinement can improve the grain boundary strengthening ($\Delta\sigma_{gs}$) in the as-extruded magnesium alloys, according to the Hall-Petch relationship [3,40,41]:

$$\Delta\sigma_{gs} = kd^{-1/2} \quad (3)$$

where *k* is the proportional constant, and *d* is the grain size. Thus, it can be deduced that the fine grains attributed to Sm addition enhance the YS significantly via grain boundary strengthening. Furthermore, amounts of much finer intermetallic particles distributed homogenously inside α-Mg matrix can effectively pin the grain boundary and impede dislocation movement during deformation. This phenomenon was frequently reported in literatures [33,38]. Hence, numerous dispersed fine particles attributed to Sm addition can contribute to the improved strength via dispersion strengthening. In addition, texture strengthening is one of the most important strengthening mechanisms in the as-extruded Mg alloy [9,10,38,42]. In the present as-extruded alloys, the basal texture was weakened gradually by Sm content increases. It reveals that the effect of texture strengthening is reduced in the as-extruded Sm-containing alloys. From the above discussion, it is evident that Sm addition can significantly enhance the strength of the as-extruded Mg–0.5Zn–0.5 Zr alloy at room temperature, mainly attributed to the grain boundary strengthening and dispersion strengthening.

4. Conclusions

(1) The fraction of intermetallic compounds increases gradually with increasing Sm content in the as-cast Mg–0.5Zn–0.5 Zr alloy, resulting in a remarkable grain refinement.
(2) Mg_3Sm phase is formed in the as-cast alloys with Sm addition less than 5.0 wt%. In the as-cast alloy with 6.5 wt% Sm addition, $Mg_{41}Sm_5$ phase is observed instead of Mg_3Sm phase. The precipitation of Mg_3Sm phase occurs in the alloy with 6.5 wt% Sm during hot extrusion, although the primary intermetallic phase is still $Mg_{41}Sm_5$.
(3) The dispersed large particles induced by Sm addition can act as heterogeneous nucleation sites for dynamic recrystallization, consequently promote DRX during hot extrusion via PSN mechanism. The weakening of basal texture in the as-extruded alloys can be explained by the increased amount of DRX grains with Sm content increases.
(4) Sm addition can significantly improve room temperature strength of the as-extruded Mg–0.5Zn–0.5 Zr alloy. The dominant strengthening mechanisms include grain boundary strengthening and dispersion strengthening.

Acknowledgements

This work was supported financially by the National Natural Science Foundation of China (Nos. 51701200 and 21601017) and the Project for Science & Technology Development of Jilin Province (Nos. 2016YHZ0006, 20170414001GH, 20180520004JH and 20180520160JH).

References

[1] X.J. Wang, D.K. Xu, R.Z. Wu, X.B. Chen, Q.M. Peng, L. Jin, Y.C. Xin, Z.Q. Zhang, Y. Liu, X.H. Chen, G. Chen, K.K. Deng, H.Y. Wang, J. Mater. Sci. Technol. 34 (2018) 245–247.
[2] C.Y. Zhao, X.H. Chen, F.S. Pan, J.F. Wang, S.Y. Gao, T. Tu, C.Q. Liu, J.H. Yao, A. Atrens, J. Mater. Sci. Technol. 35 (2019) 142–150.
[3] W.K. Wang, W.Z. Chen, W.C. Zhang, G.R. Cui, E.D. Wang, J. Mater. Sci. Technol. 34 (2018) 2042–2050.
[4] Q. Yang, K. Guan, B.S. Li, S.H. Lv, F.Z. Meng, W. Sun, Y.Q. Zhang, X.J. Liu, J. Meng, Mater. Charact. 132 (2017) 381–387.
[5] Q. Yang, K. Guan, B.S. Li, F.Z. Meng, S.H. Lv, Z.J. Yu, X.H. Zhang, J.Q. Zhang, J. Meng, J. Alloys Compd. 766 (2018) 902–907.
[6] Q. Yang, X. Qiu, S.H. Lv, F.Z. Meng, K. Guan, B.S. Li, D.P. Zhang, Y.Q. Zhang, X.J. Liu, J. Meng, Mater. Sci. Eng. A 716 (2018) 120–128.
[7] X.Y. Xia, W.H. Sun, A.A. Luo, D.S. Stone, Acta Mater. 111 (2016) 335–347.
[8] X.Y. Xia, A. Sanaty-Zadeh, C. Zhang, A.A. Luo, X.Q. Zeng, Y.A. Chang, D.S. Stone, J. Alloys Compd. 593 (2014) 71–78.
[9] K. Liu, J.X. Liu, S.B. Li, Z.H. Wang, W.B. Du, Q.F. Wang, Trans. Nonferrous Met. Soc. China 28 (2018) 890–895.

[10] X.B. Zheng, W.B. Du, Z.H. Wang, S.B. Li, K. Liu, X. Du, Mater. Lett. 212 (2018) 155–158.
[11] G.Q. Li, J.H. Zhang, R.Z. Wu, Y. Feng, S.J. Liu, X.J. Wang, Y.F. Jiao, Q. Yang, J. Meng, J. Mater. Sci. Technol. 34 (2018) 1076–1084.
[12] S.H. Lv, Y.W. Li, X.L. Lü, F.Z. Meng, Q. Yang, D.M. Han, Q. Duan, J. Meng, J. Alloys Compd. 731 (2018) 612–619.
[13] N. Tahreen, D.F. Zhang, F.S. Pan, X.Q. Jiang, D.Y. Li, D.L. Chen, J. Mater. Sci. Technol. 34 (2018) 1110–1118.
[14] B.S. Li, K. Guan, Q. Yang, X.D. Niu, D.D. Zhang, Z.J. Yu, X.H. Zhang, Z.M. Tang, J. Meng, J. Alloys Compd. 763 (2018) 120–133.
[15] J.F. Nie, X. Gao, S.M. Zhu, Scr. Mater. 53 (2005) 1049–1053.
[16] T. Honma, T. Ohkubo, S. Kamado, K. Hono, Acta Mater. 55 (2007) 4137–4150.
[17] J.H. Li, J. Barrirero, G. Sha, H. Aboulfadl, F. Mücklich, P. Schumacher, Acta Mater. 108 (2016) 207–218.
[18] K. Guan, Q. Yang, F.Q. Bu, X. Qiu, W. Sun, D.P. Zhang, T. Zheng, X.D. Niu, X.J. Liu, J. Meng, Mater. Sci. Eng. A 703 (2017) 97–107.
[19] K. Guan, B.S. Li, Q. Yang, X. Qiu, Z. Tian, D.D. Zhang, D.P. Zhang, X.D. Niu, W. Sun, X.J. Liu, J. Meng, J. Alloys Compd. 735 (2018) 1737–1749.
[20] Q. Yang, F.Q. Bu, X. Qiu, Y.D. Li, W.R. Li, W. Sun, X.J. Liu, J. Meng, J. Alloys Compd. 665 (2016) 240–250.
[21] R.G. Li, R.L. Xin, A. Chapuis, Q. Liu, G.Y. Fu, L. Zong, Y.M. Yu, B.T. Guo, S.G. Guo, Mater. Charact. 112 (2016) 81–86.
[22] K. Guan, B.S. Li, Q. Yang, D.D. Zhang, X.H. Zhang, J.Q. Zhang, L. Zhao, X.J. Liu, J. Meng, Mater. Charact. 145 (2018) 329–336.
[23] Q. Yang, K. Guan, X. Qiu, D.P. Zhang, S.H. Lv, F.Q. Bu, Y.Q. Zhang, X.J. Liu, J. Meng, Mater. Sci. Eng. A 675 (2016) 396–402.
[24] M. Sun, X.Y. Hu, L.M. Peng, P.H. Fu, Y.H. Peng, Mater. Sci. Eng. A 620 (2014) 89–96.
[25] X. Su, D.J. Li, Y.C. Xie, X.Q. Zeng, W.J. Ding, Mater. Sci. Forum 748 (2013) 238–244.
[26] J. Zheng, Q.D. Wang, Z.L. Jin, T. Peng, Mater. Sci. Eng. A 527 (2010) 1677–1685.
[27] M. Yuan, Z.Q. Zheng, Mater. Sci. Technol. 30 (2014) 261–267.
[28] S.Y. Lyu, G.D. Li, T. Hu, R.X. Zheng, W.L. Xiao, C.L. Ma, Mater. Lett. 217 (2018) 79–82.
[29] D.K. Xu, L. Liu, Y.B. Xu, E.H. Han, Mater. Sci. Eng. A 420 (2006) 322–332.
[30] L.Z. Liu, X.H. Chen, F.S. Pan, Z.W. Wang, W. Liu, P. Cao, T. Yan, X.Y. Xu, Mater. Sci. Eng. A 644 (2015) 247–253.
[31] H. Yu, Y.M. Kim, B.S. You, H.S. Yu, S.H. Park, Mater. Sci. Eng. A 559 (2013) 798–807.
[32] S.R. Wang, R. Ma, L.Y. Yang, Y. Wang, Y.J. Wang, J. Mater. Sci. 46 (2011) 3060–3065.
[33] H.Y. Yu, H.G. Yan, J.H. Chen, B. Su, Y. Zheng, Y.J. Shen, Z.J. Ma, J. Alloys Compd. 586 (2014) 757–765.
[34] D. Amberger, P. Eisenlohr, M. Göken, Acta Mater. 60 (2012) 2277–2289.
[35] N. Stanford, M.R. Barnett, Mater. Sci. Eng. A 496 (2008) 399–408.
[36] H.Y. Wang, J. Rong, Z.Y. Yu, M. Zha, C. Wang, Z.Z. Yang, R.Y. Bu, Q.C. Jiang, Mater. Sci. Eng. A 697 (2017) 149–157.
[37] E.A. Ball, P.B. Prangnell, Scr. Metall. Mater. 31 (1994) 111–116.
[38] Z.J. Yu, C. Xu, J. Meng, S. Kamado, Mater. Sci. Eng. A 703 (2017) 348–358.
[39] S.H. Park, H. Yu, J.H. Bae, C.D. Yim, B.S. You, J. Alloys Compd. 545 (2012) 139–143.
[40] K. Hagihara, A. Kinoshita, Y. Sugino, M. Yamasaki, Y. Kawamura, H.Y. Yasuda, Y. Umakoshi, Acta Mater. 58 (2010) 6282–6293.
[41] Q. Yang, K. Guan, F.Q. Bu, Y.Q. Zhang, X. Qiu, T. Zheng, X.J. Liu, J. Meng, Mater. Charact. 113 (2016) 180–188.
[42] H. Yu, S.H. Park, B.S. You, Y.M. Kim, H.S. Yu, S.S. Park, Mater. Sci. Eng. A 583 (2013) 25–35.